



Experimental observation of vortex rings in a bulk magnet

Claire Donnelly ^{1,2,3 ⋈}, Konstantin L. Metlov ^{4,5 ⋈}, Valerio Scagnoli ^{2,3}, Manuel Guizar-Sicairos ³, Mirko Holler³, Nicholas S. Bingham^{2,3}, Jörg Raabe ³, Laura J. Heyderman ^{2,3}, Nigel R. Cooper ¹ and Sebastian Gliga ³ ⋈

Vortex rings are remarkably stable structures that occur in a large variety of systems, such as in turbulent gases (where they are at the origin of weather phenomena)¹, fluids (with implications for biology)², electromagnetic discharges³ and plasmas4. Although vortex rings have also been predicted to exist in ferromagnets5, they have not yet been observed. Using X-ray magnetic nanotomography6, we imaged three-dimensional structures forming closed vortex loops in a bulk micromagnet. The cross-section of these loops consists of a vortex-antivortex pair and, on the basis of magnetic vorticity (a quantity analogous to hydrodynamic vorticity), we identify these configurations as magnetic vortex rings. Although such structures have been predicted to exist as transient states in exchange ferromagnets5, the vortex rings we observe exist as static configurations, and we attribute their stability to the dipolar interaction. In addition, we observe stable vortex loops intersected by point singularities⁷ at which the magnetization within the vortex and antivortex cores reverses. We gain insight into the stability of these states through field and thermal equilibration protocols. The observation of stable magnetic vortex rings opens up possibilities for further studies of complex three-dimensional solitons in bulk magnets, enabling the development of applications based on three-dimensional magnetic structures.

In magnetic thin films, vortices are naturally occurring flux closure states in which the magnetization curls around a stable core, where the magnetization tilts out of the film plane^{8,9}. These structures have been studied extensively over past decades due to their intrinsic stability¹⁰ and their topology-driven dynamics^{11–13}, which are of both fundamental and technological¹⁴ interest. Antivortices, the topological counterpart of vortices, are distinguished from vortices by an opposite rotation of the in-plane magnetization, which is quantified by the index of the vector field (equal to the winding number of a path traced by the magnetization vector while moving in the counterclockwise direction around the core)15. Although vortices have a circular symmetry of the magnetization (Fig. 1a), antivortices only display inversion symmetry about the centre16 (Fig. 1b), resembling saddle points in the vector field. Experimental studies of magnetic vortices and antivortices have mostly been restricted to two-dimensional (2D), planar systems, in which vortex-antivortex pairs have a natural tendency to annihilate¹⁷ unless they are part of larger, stable structures, such as cross-tie walls¹⁸.

In bulk ferromagnets, the existence of transient vortex rings, which take the form of localized solitons and are analogous to

smoke rings, has been predicted⁵, but, so far, such structures have not been observed. Just as vortex rings in fluids are characterized by their vorticity, ferromagnetic vortex ring structures can be identified by considering the magnetic vorticity¹⁹. By analogy with fluid vorticity, the magnetic vorticity is a vector field, whose components are defined by^{5,19}

$$\Omega_{\alpha} = \frac{1}{8\pi} \epsilon_{\alpha\beta\gamma} \epsilon_{ijk} m_i \partial_{\beta} m_j \partial_{\gamma} m_k \tag{1}$$

where $m_i(\mathbf{r},t)$ is a component of the unit vector representing the local orientation of the magnetization $\mathbf{m} = \mathbf{M}/M_{\rm S}$, the reduced magnetization, where $M_{\rm S}$ is the saturation magnetization, α indicates the vorticity component, and $\epsilon_{\alpha\beta\gamma}$ is the Levi–Civita tensor, summed over three components x, y and z. The magnetic vorticity vector Ω represents the topological charge flux²⁰ (or skyrmion number²¹) density. Integrating the magnetic vorticity over a closed 2D surface S results in an integer value $\int_{c} \mathbf{\Omega} \cdot d\mathbf{S} = N$ corresponding to the skyrmion number, which gives the degree of mapping of the magnetization distribution to an order parameter space described by the surface of an S^2 sphere. When N=1, the target sphere is wrapped exactly once and each direction of the magnetization vector is present on the surface S. The magnetic vorticity vector Ω is therefore non-vanishing in the vicinity of the cores of vortices or antivortices, and is represented in Fig. 1a-d for vortices and antivortices with different polarizations (the polarization is the orientation of the magnetization within the core). The vorticity vector is aligned parallel to the polarization of a vortex (Fig. 1a,c) and antiparallel to the polarization of an antivortex (Fig. 1b,d), indicating that it is dependent on the direction of the magnetization in the core as well as the index of the structure. Consequently, a vortex-antivortex pair with parallel polarizations exhibit opposite vorticities, which circulate in a closed loop (Fig. 1e).

Here, we use the magnetic vorticity to locate and identify magnetization structures within a three-dimensional (3D) GdCo₂ micropillar, imaged using hard X-ray magnetic nanotomography⁶. Within the bulk of the pillar, we find two types of vorticity loops. The first is characterized by a circulating magnetic vorticity forming vortex rings, analogous to smoke rings. The cross-sections of these magnetic vortex rings consist of vortex-antivortex pairs with parallel polarizations, as illustrated in Fig. 1e. Consequently, such a pair can be smoothly transformed into a uniformly magnetized state and carries zero topological charge. The second type of loop contains singularities, or Bloch points⁷, at which the vorticity abruptly

¹Cavendish Laboratory, University of Cambridge, Cambridge, UK. ²Laboratory for Mesoscopic Systems, Department of Materials, ETH Zürich, Zürich, Switzerland. ³Paul Scherrer Institute, Villigen, Switzerland. ⁴Donetsk Institute for Physics and Engineering, Donetsk, Ukraine. ⁵Institute for Numerical Mathematics RAS, Moscow, Russia. [™]e-mail: cd691@cam.ac.uk; metlov@donfti.ru; sebastian.gliga@psi.ch

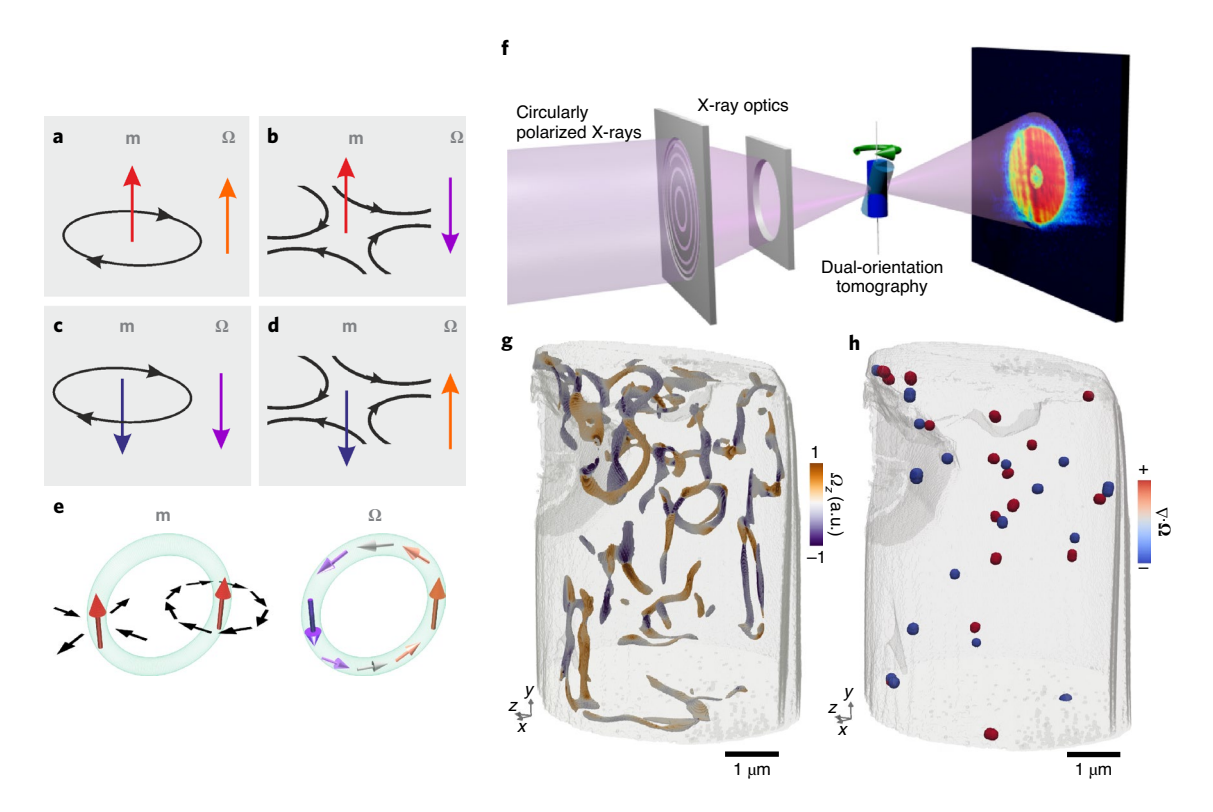


Fig. 1 | Measuring and reconstructing the magnetic structure and magnetic vorticity within a $GdCo_2$ pillar. a-d, Schematic representation of the magnetic vorticity Ω , shown in purple and orange arrows, for vortex (a,c) and antivortex (b,d) configurations with different polarizations (red, dark blue). e, The vorticity of a ring composed of a vortex-antivortex pair with parallel polarizations. f, Schematic representation of the experimental set-up: tomographic projections with magnetic contrast are measured using dichroic ptychography for the sample at many different azimuthal angles with respect to the X-ray beam (rotation indicated by the green arrow). Measurements were performed with the sample at two different tilt angles: 30° (transparent green cylinder) and 0° (blue cylinder). g,h, By plotting regions of high magnetic vorticity, we locate a variety of structures (g) and by plotting regions of high divergence of the vorticity $\nabla \cdot \Omega$, we locate Bloch points (red) and anti-Bloch points (blue), which respectively have positive and negative $\nabla \cdot \Omega$ (h).

reverses its sign, reflecting the reversal of the polarization of the vortex and antivortex within the cross-section of the ring. Calculating pre-images of the observed structures reveals concentric pre-images that do not link each other, so have a vanishing Hopf index (a topological invariant that counts the linking number of pre-images corresponding to different magnetization vector directions). In contrast, structures containing Bloch points have pre-images similar to the recently observed 'toron' structures in liquid crystals²².

The hard X-ray magnetic nanotomography set-up is shown in Fig. 1f. During the measurements, high-resolution X-ray projections of a bulk $GdCo_2$ ferrimagnetic cylinder of diameter $5\,\mu m$ were measured with dichroic ptychography²³ for 1,024 orientations of the sample with respect to the X-ray beam. The photon energy of the circularly polarized X-rays was tuned to the GdL_3 edge and, by exploiting the X-ray magnetic circular dichroism effect, sensitivity to the component of the magnetization parallel to the X-ray beam was obtained. To gain access to all three components of the magnetization, X-ray projections were measured for different sample orientations about the tomographic rotation axis for two different sample tilts. The internal magnetic structure was obtained using an iterative reconstruction algorithm⁶, which has been demonstrated to offer a robust reconstruction of nanoscale magnetic textures²⁴. Further experimental details are provided in the Methods.

In the ferrimagnetic micropillar, the coupling between two antiparallel magnetic sublattices leads to an effective soft ferromagnetic behaviour²⁵. The lowest energy state of such a magnetic cylinder is expected to consist of a single vortex²⁶. In practice, the size of the pillar is large enough to reduce the role of surface effects, supporting the stabilization of more complex, often metastable states, which can include a large number of vortices, antivortices, domain walls and singularities⁶.

We compute the magnetic vorticity Ω from the reconstructed magnetization following equation (1). Regions of large vorticity are plotted in Fig. 1g, where a number of 'tubes' and loops corresponding to the cores of vortices and antivortices are visible. In addition, unlike in incompressible fluids where the divergence must vanish, a non-zero divergence of the magnetization, M, is allowed in ferromagnets, given that Maxwell's equations only exclude the divergence of **B**. Consequently, computing the magnetic vorticity also allows us to locate singularities of the magnetization (Bloch points) within the system, which are characterized by a large divergence of the magnetic vorticity, $\nabla \cdot \Omega$, due to the abrupt local variation in the orientation of the magnetization. Here, Bloch points and anti-Bloch points are identified by positive (red) and negative (blue) $\nabla \cdot \Omega$, as plotted in Fig. 1h. Within the pillar, we find an equal number of Bloch points and anti-Bloch points, indicating that the singularities most likely originated in the bulk of the structure, where they can only be created in pairs. As a result, it appears that sample boundaries, through which a single Bloch point could be injected, did not play an essential role in the formation of the observed structures.

Within the reconstructed magnetization we observe a large number of 3D loops (Fig. 2c) that resemble the vortex ring schematically illustrated in Fig. 1e. We consider the case of one such loop, identified by plotting an isosurface corresponding to $\mathbf{m} = \pm \hat{\mathbf{x}}$ in Fig. 2a. This loop is located in the vicinity of a single vortex extending throughout the majority of the height of the pillar and whose polarization equally points along the $+\hat{\mathbf{x}}$ direction in the shown

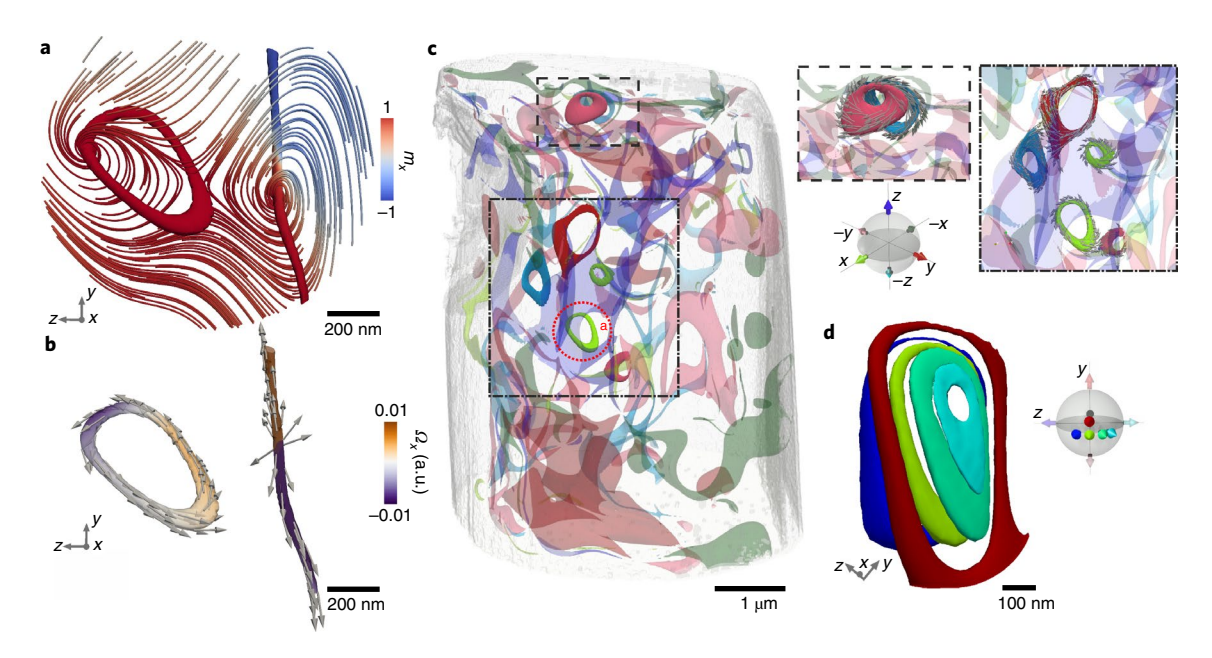


Fig. 2 | Structure of a vortex ring with circulating magnetic vorticity. **a**, A loop is identified next to a vortex by plotting an isosurface corresponding to $m_x = \pm 1$. The in-plane magnetization within a two-dimensional (2D) slice through the loop is plotted using streamlines, revealing that the cross-section of the loop consists of a vortex-antivortex pair. The colourmap indicates the value of m_x showing that the vortex and the antivortex within the loop have the same polarization. **b**, On the same $m_x = \pm 1$ isosurface, mapping the vorticity (represented both by the arrows and the colourmap) reveals that the loop exhibits a circulating vorticity and is a vortex ring. The vorticity map equally indicates that, in the nearby extended vortex, the vorticity abruptly reverses, indicating the presence of a Bloch point. Note that the plotted structures have a relatively low vorticity, with $|\Omega| \simeq 0.1$ (with the exception of the Bloch point and the extended vortex). **c**, Plotting pre-images for different directions, indicated on the schematic sphere, reveals a number of closed loops within the sample. Calculating the vorticity shows that these loops also correspond to vortex rings (insets). **d**, In the vicinity of the vortex loop plotted in **a**, pre-images for neighbouring directions are not linked, indicating a Hopf index of zero.

slice. Considering the magnetization in the y-z plane, represented by streamlines in Fig. 2a, we identify a bound state consisting of two vortices separated by an antivortex, a structure analogous to that of a cross-tie wall. Note that the streamlines are used to indicate the direction of the magnetization and are extrapolated beyond the spatial resolution of the measurements. Similarly, the isosurfaces highlight the position of the vortex core and do not represent the width of the core. The loop itself is embedded within a quasi-uniformly magnetized region ($\mathbf{m} = +\hat{\mathbf{x}}$, red) and therefore the vortex and antivortex have parallel polarizations, as shown schematically in Fig. 1e. Calculating the magnetic vorticity vector Ω , plotted in Fig. 2b, reveals a unidirectional circulation around the loop, directly comparable to the schematic in Fig. 1e. This structure is similar to a vortex ring in a fluid, which equally corresponds to a loop in the hydrodynamic vorticity. Such vorticity loops have been predicted to exist as propagating solitons in exchange ferromagnets⁵. In contrast, the loops observed here are static and stable at room temperature over the duration of our measurements. We note that the diameter of the vortex ring, that is, the average distance between the vortex and antivortex cores in the y-z plane, is ~370 nm, comparable to the diameter of other vortex rings present inside the pillar (Fig. 2c), which exhibit an average diameter of 400 ± 90 nm. Interestingly, this loop (along with a number of similar vortex rings in the sample) occurs in the vicinity of a singularity: indeed, the neighbouring vortex in the cross-tie structure contains a Bloch point, which is located in Fig. 2b where the vorticity (and the magnetization in the vortex core) abruptly reverses direction (also seen in Extended Data Fig. 1). There is, a priori, no topological requirement for the presence of a Bloch point in the proximity of the vortex loop and, despite the observed correlations, our static observations do not allow for the determination of a causal relationship between the presence of the two structures.

We gain further insight into the topology of these vortex loops by plotting pre-images corresponding to a number of directions of the magnetization in the vicinity of the vortex ring. The pre-image corresponding to the $+\hat{\mathbf{x}}$ direction, that is, $m_x = +1$, is plotted in light green in Fig. 2d, along with additional pre-images corresponding to directions indicated in the inset, which form an ensemble of closed-loop pre-images. The plotted loops do not link, indicating that the vortex ring has a Hopf index of H=0. Indeed, the vicinity of the H=0 structure contains only pre-images representing directions close to the $+\hat{\mathbf{x}}$ direction that, consequently, do not cover the S² sphere (as illustrated on the schematic sphere in Fig. 2d), meaning that the magnetization can smoothly unwind into a single point on the sphere²⁷. Hence, these vortex rings belong to a class of non-topological solitons²⁸. In the Methods (Extended Data Fig. 2c), we develop an analytic model of such a soliton, qualitatively reproducing the observed features, vorticity and pre-images.

In addition to vortex rings, we also identify loops containing sources and sinks of the magnetization due to the presence of Bloch points. The magnetic structure of one such loop, highlighted by the isosurface $m_x = \pm \hat{x}$, is shown in Fig. 3a, where the colourscale represents m_x and the magnetization in the y-z plane is represented by streamlines, revealing a vortex-antivortex pair. At two points within the loop, the polarization along the vortex and antivortex cores reverses (colour changes from blue to red). Consequently, the vorticity does not circulate around the loop, but instead assumes an asymmetric onion-like structure, flowing out from a source (green box, Fig. 3b) and into a sink (orange box, Fig. 3b). The structure of the magnetization in the vicinity of the singularities is plotted in Fig. 3c,d. The vorticity sink (Fig. 3e), whose surrounding magnetization is plotted in Fig. 3c, corresponds to a contra-circulating Bloch point²⁹ (or anti-Bloch point) with skyrmion number -1. The vorticity source (Fig. 3f) has a magnetization structure (Fig. 3d)

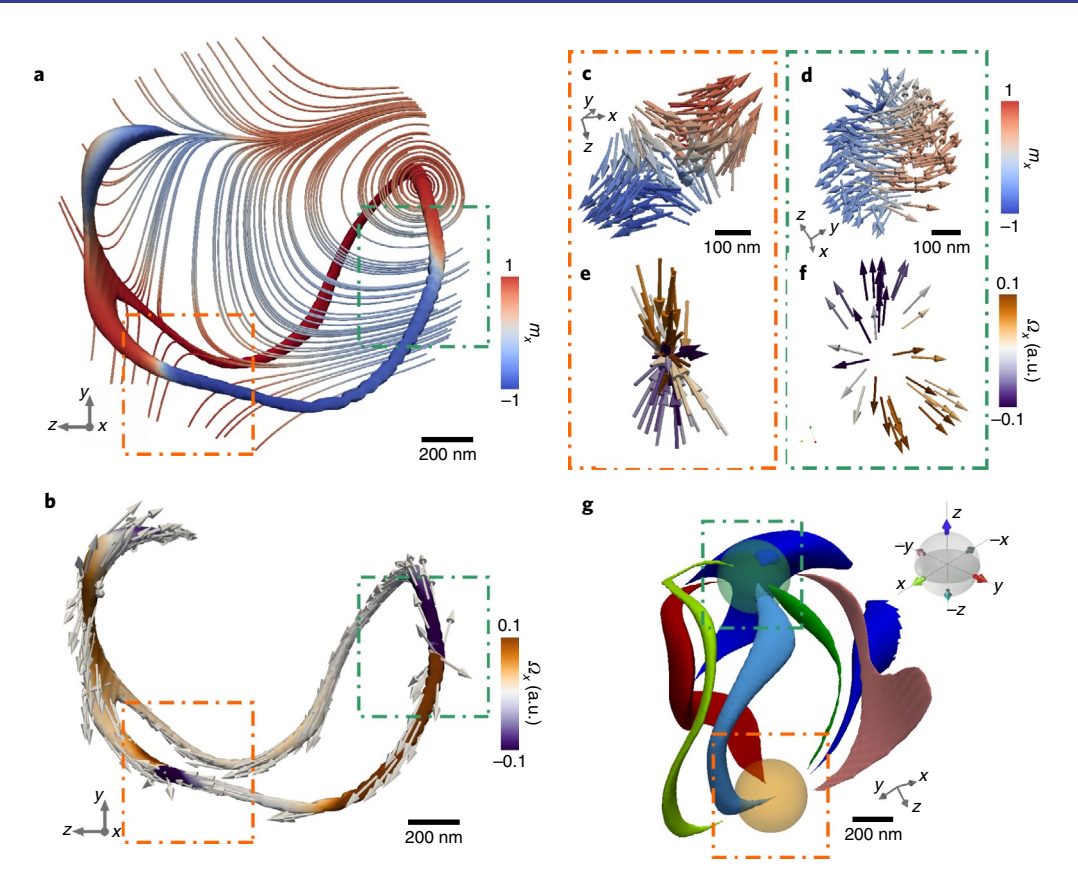


Fig. 3 | **Structure of a vortex loop containing magnetization singularities. a**, The loop is highlighted by the $m_x = \pm \hat{x}$ isosurface, while the magnetic configuration in a 2D slice is plotted using streamlines, with the colour indicating the out-of-plane magnetization component m_x . The cross-section contains a vortex-antivortex pair. Within the loop, the polarizations of the vortex and antivortex cores switch from $+m_x$ (red) to $-m_x$ (blue) at two points, indicated by the orange and green boxes. **b**, The magnetic vorticity forms an 'onion' state, with the vorticity direction reversing at the same two points. **c-f**, These locations correspond to singularities of the magnetization; their surrounding magnetic and vorticity structures are plotted in **c,d** and **e,f**, respectively. **g**, Pre-images corresponding to the Cartesian axes $\pm \hat{x}$ (light/dark green), $\pm \hat{y}$ (light/dark red) and $\pm \hat{z}$ (light/dark blue) (indicated on the schematic sphere) reveal an onion-like state, with all pre-images meeting at the singularities. See also Extended Data Fig. 4.

corresponding to that of a circulating Bloch point²⁹ with skyrmion number +1. Two features of this loop are particularly noteworthy. First, the singularities are not linked to the generation and annihilation of a vortex and antivortex with opposite polarizations, as has been reported for dynamic processes¹⁵. Instead, the loop consists of two halves connected by the Bloch points, which locally leads to a reversal of the vorticity along the vortex and the antivortex cores, as also seen in Extended Data Fig. 3. Second, while singularities have been predicted to mediate dynamic magnetization processes^{29,30} as well as to occur during magnetic field reconnection in plasma physics31, the observed structures are inherently static. In ref. 6, Bloch points were observed at the locations where a vortex core intersected a domain wall. Similarly, we find that the Bloch point pair is located at the intersection of the vortex-antivortex loop with a domain wall separating regions of opposite m_x (Extended Data Fig. 3f).

We gain further insight into the topology of the vortex–antivortex loop containing singularities by plotting pre-images corresponding to a defined set of spatial directions (or points on the S^2 sphere) in Fig. 3g. In particular, we plot regions of the magnetization aligned along $\pm \hat{\mathbf{x}}$ (bright/dark green), $\pm \hat{\mathbf{y}}$ (bright/dark red) and $\pm \hat{\mathbf{z}}$ (bright/dark blue), which form a 3D onion state, with all directions of the magnetization meeting at the singularities schematically indicated by green (Bloch point) and orange (anti-Bloch point) circles. The pre-images resemble those found to correspond to 'torons', which have recently been observed in chiral liquid crystals²²

and anisotropic fluids³². In the Methods, we present an analytical model describing different micromagnetic configurations with similar pre-images, allowing us to reproduce and, consequently, understand the experimental observations.

We explore the stability of the observed vorticity loops by applying two different field and thermal protocols on a similar GdCo₂ micropillar and performing magnetic X-ray nanotomography at remanence following each protocol. In the first protocol, we apply a 7 T magnetic field along the long axis of the pillar at room temperature and image the resulting remanent configuration. The applied field is above the measured sample saturation field of ~2 T. A plot of the magnetic vorticity (Fig. 4a) shows a large number of vortices and antivortices, as well as magnetic singularities (shown in Extended Data Fig. 5 at remanence). Plotting pre-images corresponding to different directions of the magnetization, we observe a small number of vortex loops, two of which are shown in Fig. 4b. The presence of these vortex loops after the application of a saturating magnetic field indicates that the loops can nucleate spontaneously and therefore do not require a specific field protocol to prepare them. Second, we heat the sample to 400 K while applying a 7 T magnetic field. The sample is then field-cooled and the field is gradually removed after the sample reaches room temperature. This annealing procedure is reminiscent of those used to expel defects in single crystals to increase their purity. A plot of the vorticity, shown in Fig. 4c, shows a noticeably smaller number of structures with non-vanishing vorticity. Importantly, we do not find any

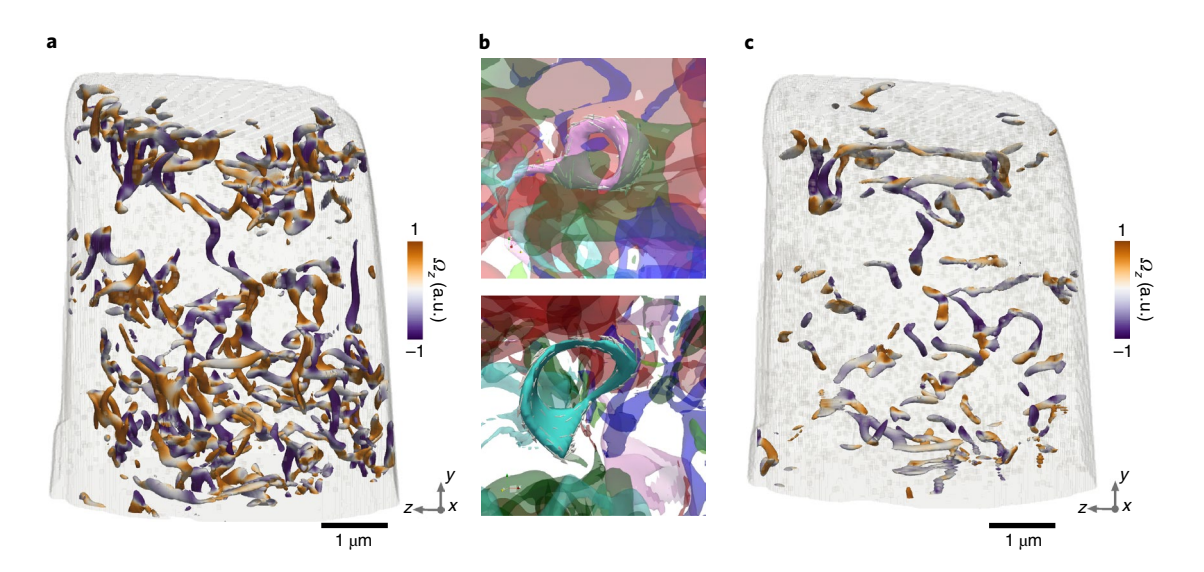


Fig. 4 | Magnetic vorticity plots measured for a similar micropillar at remanence showing the effect of different field histories. a,b, Following the application of a 7 T saturating field, a small number of vortex rings, like the one plotted in Fig. 2, are present at remanence (**a**), some of which are shown in **b. c**, After annealing in a 7 T field, followed by field cooling, no rings are observed.

vortex loops, indicating that these are metastable states that are more efficiently destroyed through thermal annealing in a field, which is likely to lead to the expulsion of magnetic as well as lattice defects that contribute to pinning of the magnetic structures (see Methods and Extended Data Figs. 6 and 7 for more details). Quantitatively, the average vorticity value following field cooling is half the value following the application of only a 7 T field, and the total number of Bloch points is roughly halved (52 versus 110 Bloch points, as seen in Extended Data Fig. 5).

Although the vortex rings we observe are topologically trivial structures and have a Hopf index of zero, they are surprisingly stable. We attribute their stability to interactions with surrounding magnetization structures, which ensure that they are, for example, embedded in cross-tie structures. In the case of the loops containing Bloch points, the singularities occur at the intersection with domain walls (as shown in Extended Data Fig. 3), thus pinning the loops. Moreover, the magnetostatic interaction clearly plays an important role in the stabilization of these structures, ensuring that our observations of stable localized solitons do not contradict the Hobart-Derrick theorem for an exchange ferromagnet that requires nonlinearities (such as intrinsic chirality in the presence of the Dzyaloshinskii-Moriya interaction) to set a scale for localized magnetization non-uniformities. Based on the balance of magnetostatic and exchange interactions, a distance of ~296 nm between the vortex and antivortex in such bound states can be estimated via the bulk limit of the cross-tie domain wall width as described in the Methods. This value matches the average observed size of the rings of 400 ± 90 nm, indicating that the balance of the magnetostatic and exchange interactions is sufficient to stabilize the structures. We note that chirality has been demonstrated in a similar bulk amorphous system through the inclusion of structural inhomogeneities³³. We expect that such systems could host topologically non-trivial solitons, such as knots with a higher Hopf index, as well as torons, following predictions for chiral magnetic heterostructures^{34–36}, analogous to the reported observations in chiral liquid crystals and ferrofluids^{27,37}.

The calculation and visualization of the magnetic vorticity and pre-images have proven essential tools in the characterization of the observed 3D structures. In combination with recent advances in time-resolved X-ray magnetic laminography³⁸, these open the path to investigating the dynamics of 3D magnetic solitons. As well as

probing resonant dynamics, it is possible that investigations of the displacement of 3D vortex rings could reveal behaviour analogous to the Kelvin motion of 2D vortex—antivortex pairs^{39–41}. Similarly, we expect that the magnetic vortex loops discovered here containing singularities will also display compelling dynamics, with implications for the fundamental understanding of the role of singularities in magnetization processes. Finally, the study of the conditions for the formation of 3D magnetic structures, and of their stability, is expected to lead to new possibilities for the controlled manipulation of the magnetization that could be relevant for technological applications requiring complexity, such as neuromorphic computing⁴² or new proposals for 3D data storage⁴³.

Online content

Any methods, additional references, Nature Research reporting summaries, source data, extended data, supplementary information, acknowledgements, peer review information; details of author contributions and competing interests; and statements of data and code availability are available at https://doi.org/10.1038/s41567-020-01057-3.

Received: 3 April 2020; Accepted: 7 September 2020; Published online: 30 November 2020

References

- Yao, J. & Lundgren, T. Experimental investigation of microbursts. *Exp. Fluids* 21, 17–25 (1996).
- Kilner, P. J. et al. Asymmetric redirection of flow through the heart. Nature 404, 759–761 (2000).
- 3. Stenhoff, M. Ball Lightning: An Unsolved Problem in Atmospheric Physics 1st edn (Springer, 1999).
- 4. Akhmetov, D. G. Vortex Rings 1st edn (Springer, 2009).
- Cooper, N. R. Propagating magnetic vortex rings in ferromagnets. *Phys. Rev. Lett.* 82, 1554–1557 (1999).
- Donnelly, C. et al. Three-dimensional magnetization structures revealed with X-ray vector nanotomography. *Nature* 547, 328–331 (2017).
- Feldtkeller, E. Mikromagnetisch Stetige und unstetige Magnetisierungskonfigurationen. Zeitschrift. Angew. Phys. 19, 530–536 (1965).
- Shinjo, T., Okuno, T., Hassdorf, R., Shigeto, K. & Ono, T. Magnetic vortex core observation in circular dots of permalloy. Science 289, 930–932 (2000).
- Wachowiak, A. et al. Direct observation of internal spin structure of magnetic vortex cores. Science 298, 577–580 (2002).
- Guslienko, K. Magnetic vortex state stability reversal and dynamics in restricted geometries. J. Nanosci. Nanotechnol. 8, 2745–2760 (2008).

- Choe, S.-B. et al. Vortex core-driven magnetization dynamics. Science 304, 420–422 (2004).
- 12. Van Waeyenberge, B. et al. Magnetic vortex core reversal by excitation with short bursts of an alternating field. *Nature* **444**, 461–464 (2006).
- 13. Hertel, R., Gliga, S., Fähnle, M. & Schneider, C. M. Ultrafast nanomagnetic toggle switching of vortex cores. *Phys. Rev. Lett.* **98**, 117201 (2007).
- Pigeau, B. et al. A frequency-controlled magnetic vortex memory. Appl. Phys. Lett. 96, 132506 (2010).
- Hertel, R. & Schneider, C. M. Exchange explosions: magnetization dynamics during vortex-antivortex annihilation. *Phys. Rev. Lett.* 97, 177202 (2006).
- Gliga, S., Yan, M., Hertel, R. & Schneider, C. M. Ultrafast dynamics of a magnetic antivortex: micromagnetic simulations. *Phys. Rev. B* 77, 060404 (2008).
- Gliga, S., Hertel, R. & Schneider, C. M. Switching a magnetic antivortex core with ultrashort field pulses. J. Appl. Phys. 103, 07B115 (2008).
- Neudert, A. et al. Bloch-line generation in cross-tie walls by fast magnetic-field pulses. J. Appl. Phys. 99, 08F302 (2006).
- Papanicolaou, N. in Singularities in Fluids, Plasmas and Optics Vol. 404 (ASI Series C404, NATO, 1993).
- Belavin, A. A. & Polyakov, A. M. Metastable states of two-dimensional isotropic ferromagnet. *ZETP Lett.* 22, 245–247 (1975).
- Senthil, T., Vishwanath, A., Balents, L., Sachdev, S. & Fisher, M. P. A. Deconfined quantum critical points. Science 303, 1490–1494 (2004).
- Ackerman, P. J. & Smalyukh, I. I. Diversity of knot solitons in liquid crystals manifested by linking of preimages in torons and hopfions. *Phys. Rev. X* 7, 011006 (2017).
- Donnelly, C. et al. High-resolution hard X-ray magnetic imaging with dichroic ptychography. Phys. Rev. B 94, 064421 (2016).
- Donnelly, C. et al. Tomographic reconstruction of a three-dimensional magnetization vector field. New J. Phys. 20, 083009 (2018).
- Chikazumi, S. in International Series of Monographs on Physics 2nd edn, Vol. 94 (Oxford Univ. Press, 2010).
- Arrott, A., Heinrich, B. & Aharoni, A. Point singularities and magnetization reversal in ideally soft ferromagnetic cylinders. *IEEE Trans. Magn.* 15, 1228–1235 (1979).
- Ackerman, P. J. & Smalyukh, I. I. Static three-dimensional topological solitons in fluid chiral ferromagnets and colloids. *Nat. Mater.* 16, 426–432 (2016).
- 28. Lee, T. & Pang, Y. Nontopological solitons. Phys. Rep. 221, 251-350 (1992).

- Malozemoff, A. & Slonczewski, J. in Magnetic Domain Walls in Bubble Materials (eds Malozemoff, A. & Slonczewski, J.) Ch. IV, 77–121 (Academic Press, 1979).
- Miltat, J. & Thiaville, A. Vortex cores—smaller than small. Science 298, 555–555 (2002).
- Kerr, R. M. & Brandenburg, A. Evidence for a singularity in ideal magnetohydrodynamics: implications for fast reconnection. *Phys. Rev. Lett.* 83, 1155–1158 (1999).
- Smalyukh, I. I., Lansac, Y., Clark, N. A. & Trivedi, R. P. Three-dimensional structure and multistable optical switching of triple-twisted particle-like excitations in anisotropic fluids. *Nat. Mater.* 9, 139–145 (2009).
- 33. Kim, D.-H. et al. Bulk Dzyaloshinskii–Moriya interaction in amorphous ferrimagnetic alloys. *Nat. Mater.* **18**, 685–690 (2019).
- 34. Liu, Y., Lake, R. K. & Zang, J. Binding a hopfion in a chiral magnet nanodisk. *Phys. Rev. B* **98**, 174437 (2018).
- 35. Sutcliffe, P. Hopfions in chiral magnets. J. Phys. A 51, 375401 (2018).
- Tai, J.-S. B. & Smalyukh, I. I. Static Hopf solitons and knotted emergent fields in solid-state noncentrosymmetric magnetic nanostructures. *Phys. Rev. Lett.* 121, 187201 (2018).
- Chen, B. G.-G, Ackerman, P. J., Alexander, G. P., Kamien, R. D. & Smalyukh, I. I. Generating the Hopf fibration experimentally in nematic liquid crystals. *Phys. Rev. Lett.* 110, 237801 (2013).
- Donnelly, C. et al. Time-resolved imaging of three-dimensional nanoscale magnetisation dynamics. Nat. Nanotechnol. 15, 356–360 (2020).
- Pokrovskii, V. L. & Uimin, G. V. Dynamics of vortex pairs in a two-dimensional magnetic material. *JETP Lett.* 41, 128 (1985).
- Papanicolaou, N. & Spathis, P. N. Semitopological solitons in planar ferromagnets. *Nonlinearity* 12, 285–302 (1999).
- Cooper, N. R. Solitary waves of planar ferromagnets and the breakdown of the spin-polarized quantum Hall effect. Phys. Rev. Lett. 80, 4554–4557 (1998).
- Huang, Y., Kang, W., Zhang, X., Zhou, Y. & Zhao, W. Magnetic skyrmion-based synaptic devices. *Nanotechnology* 28, 08LT02 (2017).
- 43. Fernández-Pacheco, A. et al. Three-dimensional nanomagnetism. *Nat. Commun.* **8**, 15756 (2017).

Publisher's note Springer Nature remains neutral with regard to jurisdictional claims in published maps and institutional affiliations.

© The Author(s), under exclusive licence to Springer Nature Limited 2020

Methods

Sample fabrication. $GdCo_2$ micropillars of diameter 5 µm were cut from a larger nugget of $GdCo_2$ using a focused ion beam in combination with a micromanipulator, and mounted on top of OMNY tomography pins⁴⁴.

The crystal structure of the GdCo₂ micropillars was determined using microcrystallography measurements performed at the X06DA beamline at the Swiss Light Source, Paul Scherrer Institute. An example diffraction pattern is given in Extended Data Fig. 6, where one can observe that the Bragg peaks display a substructure (right image), indicating the polycrystalline nature of the micropillar.

X-ray ptychographic tomography. Hard X-ray magnetic tomography was performed at the cSAXS beamline at the Swiss Light Source, Paul Scherrer Institute, using the flexible tomographic nano-imaging (flOMNI) instrument⁴⁵. Part of the data presented in this manuscript (the central vortex containing the Bloch point in Fig. 2a,b) formed part of the dataset presented in ref. ⁶. All other measurements and analysis are shown here for the first time.

Two-dimensional tomographic projections were measured with X-ray ptychography, a coherent diffractive imaging technique allowing access to the full complex transmission function of the sample 46,47 . For X-ray ptychography, an X-ray illumination of $\sim\!4\,\mu m$ was defined on the sample, and ptychography scans were performed by measuring diffraction patterns on a concentric grid of circles with a radial separation of $0.4\,\mu m$ for a field of view of $8\times7\,\mu m^2$ and $13\times9\,\mu m^2$ for the untilted and tilted sample orientations, respectively. The projections were reconstructed using 500 iterations of the difference map and 200 iterations of the maximum likelihood refinement using the cSAXS PtychoShelves package 48 .

To probe the magnetization of the sample, X-rays tuned to the Gd L_3 edge with a photon energy of 7.246 keV were chosen to maximize the absorption X-ray magnetic circular dichroism signal²³. Circularly polarized X-rays were produced by including a 500- μ m-thick diamond phase plate upstream of the sample position⁴⁹. The degree of circular polarization achieved was greater than 99%, with a transmission of ~35%.

The tomographic projections were aligned with high precision as described in ref. $^6\!.$

Magnetic tomography. When a single circular polarization projection is measured, the component of the magnetization parallel to the X-ray beam is probed via X-ray magnetic circular dichroism, along with the electronic structure of the sample. To probe all three components of the magnetization, projections were measured around a rotation axis for two orientations of the sample⁶. Generally, the magnetic contrast of a projection is isolated from other contrast mechanisms by measuring the same projection using circularly left- and right-polarized light, where the sign of the magnetic contrast is reversed, and taking the difference between the two images. Here, a single X-ray polarization was used for all measurements and, to isolate the magnetic structure, projections with circularly left polarization were measured at θ and θ + 180°. Between these two angles, the magnetic contrast is reversed; this can be used to differentiate the magnetic contrast from the electronic contrast. Accordingly, for the magnetic tomography measurements, circular left polarization projections were measured through 360° about the rotation axis, instead of through 180°, as in standard tomography.

The magnetization (which is a 3D vector field) was reconstructed using a two-step gradient-based iterative reconstruction algorithm, as described in ref. ⁵⁰. The spatial resolution for each component of the magnetization was estimated using Fourier shell correlation ⁵¹, and a 3D Hanning low-pass filter was used to remove high-frequency noise. The spatial resolution of the reconstructed magnetization was found to be 97 nm, 125 nm and 127 nm in the x–z, x–y and y–z planes, respectively.

The magnetic vorticity was calculated according to equation (1). The magnetization was normalized to obtain the unit vector, which was used to calculate the magnetic vorticity numerically in MATLAB. Specifically, the components of the vorticity vector were calculated numerically as follows:

$$\begin{split} \Omega_{x} &= 2m_{x}(\partial_{y}m_{y}\partial_{z}m_{z} - \partial_{z}m_{y}\partial_{y}m_{z}) + 2m_{y}(\partial_{y}m_{z}\partial_{z}m_{x} - \partial_{z}m_{z}\partial_{y}m_{x}) \\ &\quad + 2m_{z}(\partial_{y}m_{x}\partial_{z}m_{y} - \partial_{z}m_{x}\partial_{y}m_{y}) \\ \Omega_{y} &= 2m_{x}(\partial_{z}m_{y}\partial_{x}m_{z} - \partial_{x}m_{y}\partial_{z}m_{z}) + 2m_{y}(\partial_{z}m_{z}\partial_{x}m_{x} - \partial_{x}m_{z}\partial_{z}m_{x}) \\ &\quad + 2m_{z}(\partial_{z}m_{x}\partial_{x}m_{y} - \partial_{x}m_{x}\partial_{z}m_{y}) \\ \Omega_{z} &= 2m_{x}(\partial_{x}m_{y}\partial_{y}m_{z} - \partial_{y}m_{y}\partial_{x}m_{z}) + 2m_{y}(\partial_{x}m_{z}\partial_{y}m_{x} - \partial_{y}m_{z}\partial_{x}m_{x}) \\ &\quad + 2m_{z}(\partial_{x}m_{x}\partial_{y}m_{y} - \partial_{y}m_{x}\partial_{x}m_{y}) \end{split} \tag{2}$$

where m_i is the *i*th component of the reduced magnetization and ∂_i represents the partial derivative with respect to the *i*th direction that were calculated numerically using the gradient function in MATLAB 2018a.

The 3D visualizations of the magnetic vorticity and magnetization were performed with Paraview⁵². To consider the topology of the magnetization in three dimensions, pre-images corresponding to different directions are plotted within the pillar. The difference between the magnetization vector and the m_x =1 direction is calculated using

$$\delta_{px} = \left(\frac{m_x}{|\mathbf{m}|} - 1\right)^2 + \left(\frac{m_y}{|\mathbf{m}|}\right)^2 + \left(\frac{m_z}{|\mathbf{m}|}\right)^2 \tag{3}$$

To plot the m_x = 1 pre-image, for example, we plot an isosurface for $\delta_{\rm px}$ = 0.01. This results in a tube rather than a line, which is necessary due to the finite spatial resolution and signal-to-noise ratio of the measurement.

Field and thermal protocols. A separate $GdCo_2$ micropillar was used to investigate the effect of two different protocols, and the magnetic state was determined using magnetic tomography. The first protocol involved the application of a 7 T saturating field at room temperature. The second involved thermal annealing (heating the micropillar to a temperature of 400 K close to the Curie temperature of the material), applying a 7 T field and then reducing the temperature to room temperature, followed by a slow reduction of the applied magnetic field.

In the final states, a notable difference in both the presence of high-vorticity structures as well as the number of Bloch points was observed. This can be seen in Fig. 4 and Extended Data Fig. 5, with the thermal annealing procedure resulting in a large decrease in the average magnetic vorticity as well as in the number of Bloch points.

We note that, although the general magnetic structure is significantly different following the different protocols, and a large reduction in the average magnetic vorticity is observed following the annealing process, the main vortex that spans most of the height of the pillar occupies a similar position, within $\sim\!300\,\mathrm{nm}$, as can be seen in Extended Data Fig. 7. Given that the vortex state is, in principle, the ground state of a cylindrical sample, the formation of the vortex core at nearby locations in a structure of this size is indicative of the presence of pinning centres that may be attributed to the polycrystalline nature of the material. The suppression of high-vorticity structures, as well as magnetic vortex rings, following the thermal annealing protocol (Extended Data Fig. 5) indicates, however, that the pinning centres do not solely determine the stability of the structures, but rather may indirectly influence them through the pinning of neighbouring magnetic features

Analytical models. To qualitatively interpret and understand the observed structures, we build a series of 2+1 dimensional models, which allow us to compare the observed magnetization structures, pre-images and vorticity with those derived from modelled vortex loops with different magnetization structures. These models are similar to those used to describe hopfions in ref. ⁵³. They are based on the subdivision of the magnetic material volume into thin slices, lying in the x-y plane of a Cartesian coordinate system. The magnetization in each slice can then be described by a complex function w of a complex variable u=x+iy by means of stereographic projection $\{m_x+im_y,m_z\}=\{2w,1-w\overline{w}\}/(1+w\overline{w})$, where the overline denotes complex conjugation, so that $\overline{u}=x-iy$, $i=\sqrt{-1}$. Without loss of generality, any 3D magnetization distribution $\mathbf{m}(x,y,z)$ can be described by a function $w=w(u,\overline{u},z)$, which depends on the complex coordinate u within each slice and the extra-dimensional variable z, identifying the slice.

For realistic models, including at least the exchange and the magnetostatic interactions, no exact solutions for non-uniform $w(u,\overline{u},z)$ are known. However, if the magnetostatic interaction is neglected and $w(u,\overline{u},z)$ is assumed to be weakly dependent on z, two large families of exact solutions exist for $w(u,\overline{u},z)$ at a fixed z. These are solitons²⁰, which are meromorphic functions $w(u,\overline{u},z)=f(u,z)$, and singular merons²⁴, which are functions with $|w(u,\overline{u},z)|=1$ or $w(u,\overline{u},z)=f(u,z)/|f(u,z)|$. Zeros of f(u,z) correspond to the centres of magnetic vortices (or hedgehog-like structures, if the magnetization vectors are rotated by $\pi/2$ in the x-y plane). The poles correspond to the centres of the magnetic antivortices (or saddles). From the stereographic projection it follows that, for solitons, $m_z=1$ in the centres of the vortices and $m_z=-1$ in the centres of antivortices.

An example of meromorphic functions are the rational functions of a complex argument (quotient of two polynomials). They allow direct expression of the vortex/antivortex pair annihilation as a cancellation of two identical monomials, whereas creation is a time-reversed process. The topological charge (or skyrmion number) in each slice is a conserved quantity²⁰ in the sense that it cannot be changed by a smooth singularity-free variation of the magnetization distribution. For the slices in the x-y plane, the topological charge density is the z-component of the vorticity Ω_z and the total charge is the integral of this density over the whole slice. Creation and annihilation of the vortex—antivortex pairs within the soliton is always accompanied by a singularity.

A vortex ring can be understood as a process of creation, separation, convergence and annihilation of a vortex–antivortex pair as the variable z advances through successive slices⁵. Consider

$$w_{\rm BPr}(u, \overline{u}, z) = f(u, z) = i \frac{u - p(z)}{u + p(z)} = i \frac{u - \sqrt{1 - (z/2)^2}}{u + \sqrt{1 - (z/2)^2}}$$
(4)

for an (arbitrary) range -2 < z < 2, where the specific expression for p(z) was chosen to make the vortex and antivortex cores extend along arcs, as in the experimental data. It describes the creation of a vortex–antivortex pair at x = y = 0

and z=2, the vortex and antivortex moving apart (with the maximum distance between their centres equal to 2 at z=0), then approaching each other again, and annihilating at z=-2. We call this model the Belavin–Polyakov ring (BPr) because each slice is a Belavin–Polyakov soliton, described by a meromorphic $w(u, \overline{u}, z)$. The corresponding schematic magnetization, set of pre-images and vorticity are shown in Extended Data Fig. 2a. A similar pre-image pattern connecting two Bloch points was indeed observed in our sample. However, the corresponding vorticity distributions are different. Indeed, instead of a single centrally symmetric vorticity bundle we reconstruct a pair of bundles, corresponding to the vortex and antivortex centres. Clearly, the pure Belavin–Polyakov ring model cannot reproduce this feature.

To 'unbundle' the vortex and antivortex, we can use the instanton model⁵⁴ by writing

$$w_{i}(u, \overline{u}, z) = \begin{cases} f(u, z)/c(z) & |f(u, z)| \le c(z) \\ f(u, z)/|f(u, z)| & d(z) > |f(u, z)| > c(z) \\ f(u, z)/d(z) & |f(u, z)| > d(z) \end{cases}$$
(5)

where d(z)=1/c(z), assuming the same size for the vortex and antivortex cores. Choosing c(z)=1-q+q|z|/2<1 allows control of the size of the vortex and antivortex cores (where $m_z\neq 0$) at the central plane z=0 via the parameter q. The magnetization, pre-images and vorticity for such an instanton ring with q=3/4 are shown in Extended Data Fig. 2b. Although they reproduce qualitatively both the vorticity distribution and the pre-images, shown in Fig. 3b,g, the structure of the Bloch points is different. Indeed, the instanton ring has two hedgehog-type Bloch points (in which the magnetization directions are opposite), whereas the observed structure, shown in Fig. 3, contains two different types of Bloch point. Additionally, this model differs from the observation in Fig. 3 in that singularities are absent at the transition from the experimentally observed vortex and antivortex pair to a uniformly magnetized region. The Bloch points in Fig. 3 instead coincide with the polarization reversal of the vortex and antivortex cores as they propagate through the volume of the sample. To analytically describe this structure, we first need to build a model for a vortex ring.

To describe a vortex–antivortex pair unbound by Bloch point singularities, the vortex and antivortex must have identical polarizations (that is, the same direction of m_z within the core). In this case the topological charge in each slice is zero. Such a configuration can be obtained as a generalization of equation (5):

$$w_{\rm r}(u, \overline{u}, z) = A(z) \begin{cases} f(u, z)/c(z) & |f(u, z)| \le c(z) \\ f(u, z)/|f(u, z)| & d(z) > |f(u, z)| > c(z) \\ d(z)/\overline{f(u, z)} & |f(u, z)| > d(z) \end{cases} \tag{6}$$

where the modification to the last line reverses the polarization of the antivortex. The factor $A(z)=(1-z^2/4)s$ ensures that, at $z=\pm 2$, the function $w_r=0$, which corresponds to the uniform state. The parameter s allows for control of the degree of quasi-uniformity: the smaller s is, the less m_s deviates from 1. The magnetization, pre-images and vorticity for such a quasi-uniform ring with q=3/4 and s=1/4 are shown in Extended Data Fig. 2c. They are qualitatively analogous to the experimentally observed vortex rings in Fig. 2b,d.

Finally, we can extend the above model to a vortex ring in which the polarization reverses along the vortex and antivortex cores, in the presence of Bloch points. To describe this state, we note that with s=1, $c(z)=z^2/4$, the magnetization of the quasi-uniform ring (equation (6)) at z=0 lies completely in the x-y plane except for at the centres of the vortex and antivortex, where its direction is undefined. Joining at the central plane two half-rings with opposite polarizations gives

$$w_{\text{vls}}(u, \overline{u}, z) = A(z) \begin{cases} w_{\text{r}}(u, \overline{u}, z) & z \le 0\\ 1/\overline{w_{\text{r}}(u, \overline{u}, z)} & z > 0 \end{cases}$$
 (7)

which yields the model for the vortex loop with Bloch point singularities, shown in Extended Data Fig. 2d. The structure corresponds well to the observations in Fig. 3, including the observed Bloch point types.

Note that, despite the piecewise nature of the above functions, the resulting magnetization vector fields are continuous (apart from at the singularities). Although neither ansatz in the presented series is an exact solution of the corresponding micromagnetic problem (not even of its restricted exchange-only version), they provide a simple and easily interpretable model to understand the observed magnetization distributions.

We now address the question of the size of the observed magnetization structures. According to the Hobart–Derrick theorem, the exchange interaction alone cannot stabilize the solitons as the exchange energy does not display a minimum as a function of soliton size. However, the magnetostatic interaction (which is outside the scope of the Hobart–Derrick theorem) can, in principle, set the length scale of solitons. A complete answer to this question requires a sophisticated theoretical model, which still remains an open problem. Yet, a simple argument for the stability of the observed bound states can be given in terms of other well-known magnetic textures such as a cross-tie wall as described below.

A single magnetic vortex, centred in a cylindrical nanopillar, does not give rise to magnetic volume charges (which are proportional to the divergence of the magnetization) and only generates surface charges (proportional to the magnetization vector component, normal to the surface) in the region of the core at the surfaces of the pillar. The total energy (exchange plus surface magnetostatic) of the magnetic vortex has a minimum when varying the vortex core size. However, as the length of the pillar is increased to infinity, the equilibrium vortex core size diverges due to the diminishing role of the surfaces. In finite pillars, the vortex core has a barrel-like shape that is narrow at the top/bottom surfaces and wide in the middle of the pillar. However, these surface charges do not explain the stability of the structures in the bulk of our pillar, which do not extend to the surfaces of the sample.

It is well known that, in thin films, vortices and antivortices can form bound states, such as in cross-tie walls⁵⁶. A simple theoretical model for such a wall can be given directly in terms of the complex function w of a (complex) variable u (ref. ⁵⁷):

$$w_{c-t}(u, \overline{u}, z) = i \tan(u/s) \tag{8}$$

where s is the spatial scale (width) of the domain wall. The corresponding magnetization structure has both volume and surface magnetic charges. The magnetostatic energy associated to these charges stabilizes the wall, yielding a certain equilibrium value of s as a function of the film thickness L and the exchange length $L_{\rm EX} = \sqrt{2A/(\mu_0 M_{\rm S}^2)}$, where A is the exchange constant of the material, μ_0 is the vacuum permeability and $M_{\rm S}$ the saturation magnetization. It should be noted, however, that, due to the presence of magnetic volume charges, the domain wall width for the model given by equation (8) does not diverge as the film thickness goes to infinity $L \to \infty$, but assumes a finite bulk limit:

$$s_{\infty} = 8\sqrt{\frac{3}{12 - \pi^2}} L_{\text{EX}}$$
 (9)

which can be directly computed using the magnetostatic function for the cross-tie wall⁵⁷. For GdCo₂ with an exchange length $L_{\rm EX} \simeq 20$ nm, the resulting value of $s_{\infty} \simeq 189$ nm, corresponding to the distances between the vortex and antivortex centres of $s_{\infty}\pi/2 \simeq 296$ nm, can serve as a ballpark theoretical estimate for the size of vortex rings.

Unlike a cross-tie domain wall, the magnetic vortex rings we observe are quasi-uniform states and exist as a perturbation of a mostly uniform background. Because the magnetization vector is included in both the exchange energy (squared gradients of components) and the magnetic volume charges density (product of divergences) via derivatives, a constant background is irrelevant and we can roughly assume that, in the quasi-uniform state, only the spatial variation of the magnetization vector is reduced compared to the case of fully developed vortices and antivortices. For the quasi-uniform cross-tie domain wall, this can be modelled by representing its total energy as

$$E_{\rm c-t} \propto c_1 \frac{(L_{\rm EX}/L)^2}{s} + c_2 F(s)$$
 (10)

where the case $c_1 = c_2 = 1$ corresponds to the energy of the fully developed cross-tie wall³⁷ and F(s) is the magnetostatic function. The parameters c_1 and c_2 then account for the reduced variation of the magnetization in the quasi-uniform case, which has different effects on the exchange and magnetostatic energy terms. It is important to note that, provided $c_1, c_2 \neq 0$, this reduced variation does not destroy the energy minimum for s, but merely rescales the equilibrium wall width. This means that the quasi-uniform bound state of vortices and antivortices can also be stable with respect to scaling, as for the cross-tie wall in a bulk magnet.

Data availability

Experimental data and analysis codes used for this manuscript can be found at https://doi.org/10.5281/zenodo.4041745.

References

- Holler, M. et al. OMNY PIN—a versatile sample holder for tomographic measurements at room and cryogenic temperatures. *Rev. Sci. Instrum.* 88, 113701 (2017).
- Holler, M. et al. High-resolution non-destructive three-dimensional imaging of integrated circuits. *Nature* 543, 402–406 (2017).
- 46. Pfeiffer, F. X-ray ptychography. Nat. Photon. 12, 9-17 (2017).
- 47. Rodenburg, J. M. et al. Hard-X-ray lensless imaging of extended objects. *Phys. Rev. Lett.* **98**, 034801 (2007).
- Wakonig, K. et al. PtychoShelves, a versatile high-level framework for high-performance analysis of ptychographic data. J. Appl. Crystallogr. 53, 574–586 (2020)
- Scagnoli, V. et al. Linear polarization scans for resonant X-ray diffraction with a double-phase-plate configuration. J. Synch. Radiat. 16, 778–787 (2009).
- Donnelly, C. Hard X-ray Tomography of Three Dimensional Magnetic Structures. PhD thesis, ETH Zurich (2017).

- van Heel, M. & Schatz, M. Fourier shell correlation threshold criteria. J. Struct. Biol. 151, 250–262 (2005).
- 52. Ahrens, J., Geveci, B. & Law, C. ParaView: An End-User Tool for Large Data Visualization. Visualisation Handbook (Elsevier, 2005).
- 53. Wilczek, F. & Zee, A. Linking numbers, spin and statistics of solitons. *Phys. Rev. Lett.* **51**, 2250–2252 (1983).
- 54. Gross, D. J. Meron configurations in the two-dimensional O(3) σ -model. *Nucl. Phys. B* **132**, 439–456 (1978).
- Usov, N. A. & Peschany, S. E. Magnetization curling in a fine cylindrical particle. J. Magn. Magn. Mater. 118, L290–L294 (1993).
- Huber, E. E., Smith, D. O. & Goodenough, J. B. Domain-wall structure in permalloy films. J. Appl. Phys. 29, 294–295 (1958).
- Metlov, K. L. Simple analytical description of the cross-tie domain wall structure. Appl. Phys. Lett. 79, 2609–2611 (2001).

Acknowledgements

X-ray magnetic tomography measurements were performed at the cSAXS beamline at the Swiss Light Source, Paul Scherrer Institute (PSI), Switzerland, and X-ray microcrystallography measurements at the X06DA beamline at the Swiss Light Source, PSI, Switzerland. We thank A. Bogatyrëv for his careful reading of the manuscript and valuable remarks, R. Cowburn for discussions and V. Olieric for microcrystallography measurements. We thank R. M. Galera for providing and performing magnetic characterizations of the GdCo₂ nugget, S. Stutz for the sample fabrication and E. Müller from the Electron Microscopy Facility at PSI for the focused ion beam preparation of the pillar samples. C.D. is supported by the Leverhulme Trust (ECF-2018-016), the Isaac Newton Trust (18-08) and the L'Oréal-UNESCO UK and Ireland Fellowship for Women in Science. S.G. was funded by the Swiss National Science Foundation, Spark project

no. 190736. K.L.M. acknowledges the support of the Russian Science Foundation under project no. RSF 16-11-10349. N.R.C. was supported by EPSRC grant EP/P034616/1 and by a Simons Investigator Award.

Author contributions

The study of topological magnetic features in three dimensions was conceived by S.G., C.D. and K.L.M., and originated from a larger project on 3D magnetic systems conceived by L.J.H. and J.R. C.D., M.G.-S., S.G., V.S., M.H. and J.R. performed the experiments. Magnetometry measurements of the material were performed by N.S.B. and V.S. C.D. performed the magnetic reconstruction with support from M.G.-S. and V.S. C.D. analysed the data and N.R.C. conceived the calculation of the magnetic vorticity. C.D., K.L.M., N.R.C. and S.G. interpreted the magnetic configuration. K.L.M. developed the analytical model. C.D., K.L.M., N.R.C. and S.G. wrote the manuscript with contributions from all authors.

Competing interests

The authors declare no competing interests.

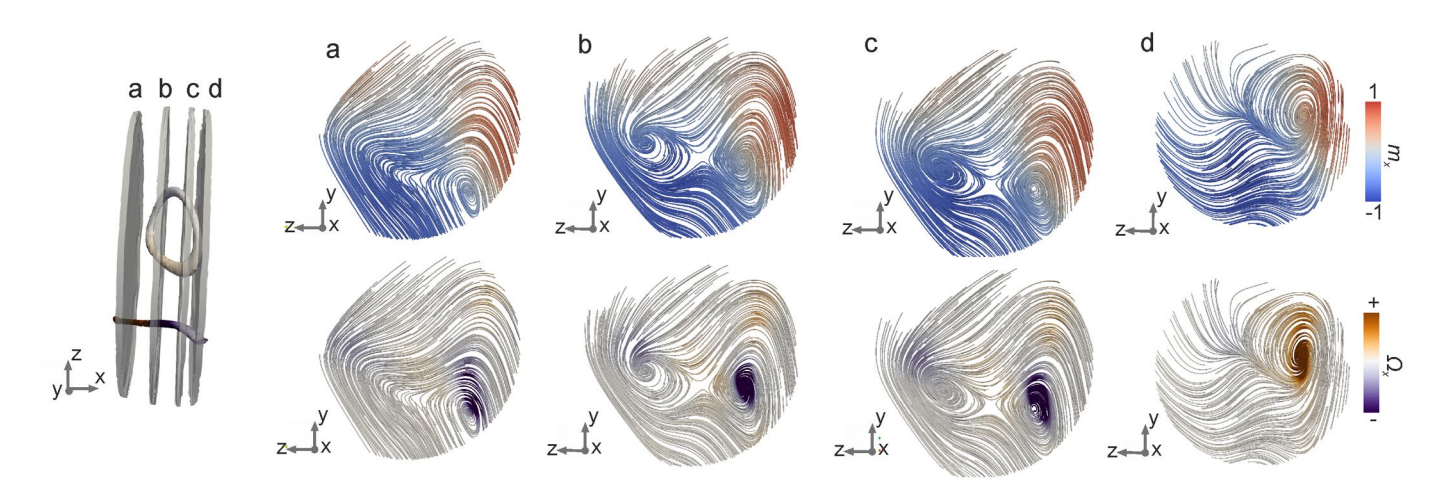
Additional information

Extended data is available for this paper at https://doi.org/10.1038/s41567-020-01057-3.

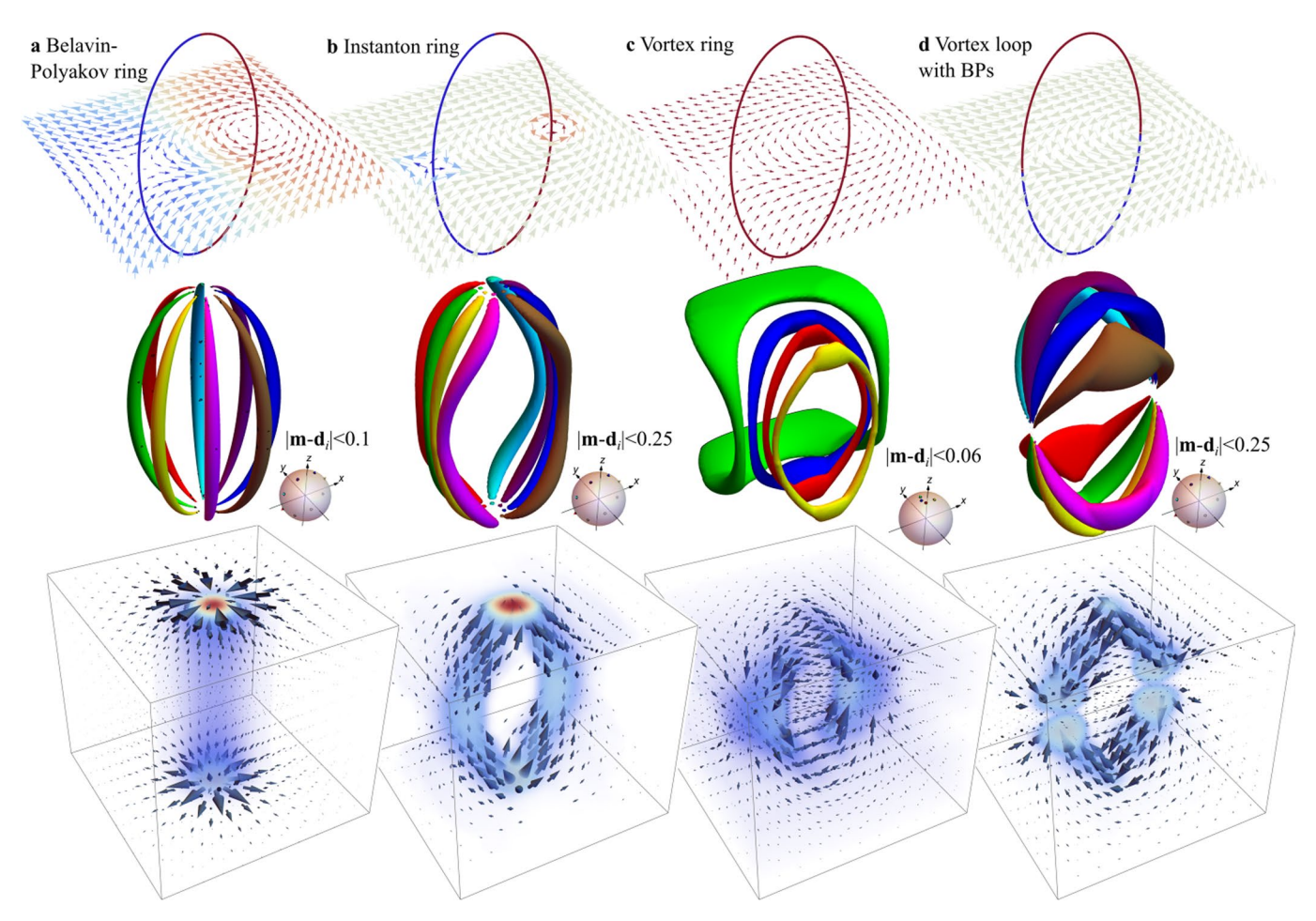
Correspondence and requests for materials should be addressed to C.D., K.L.M. or S.G.

Peer review information *Nature Physics* thanks Paul Sutcliffe and the other, anonymous, reviewer(s) for their contribution to the peer review of this work.

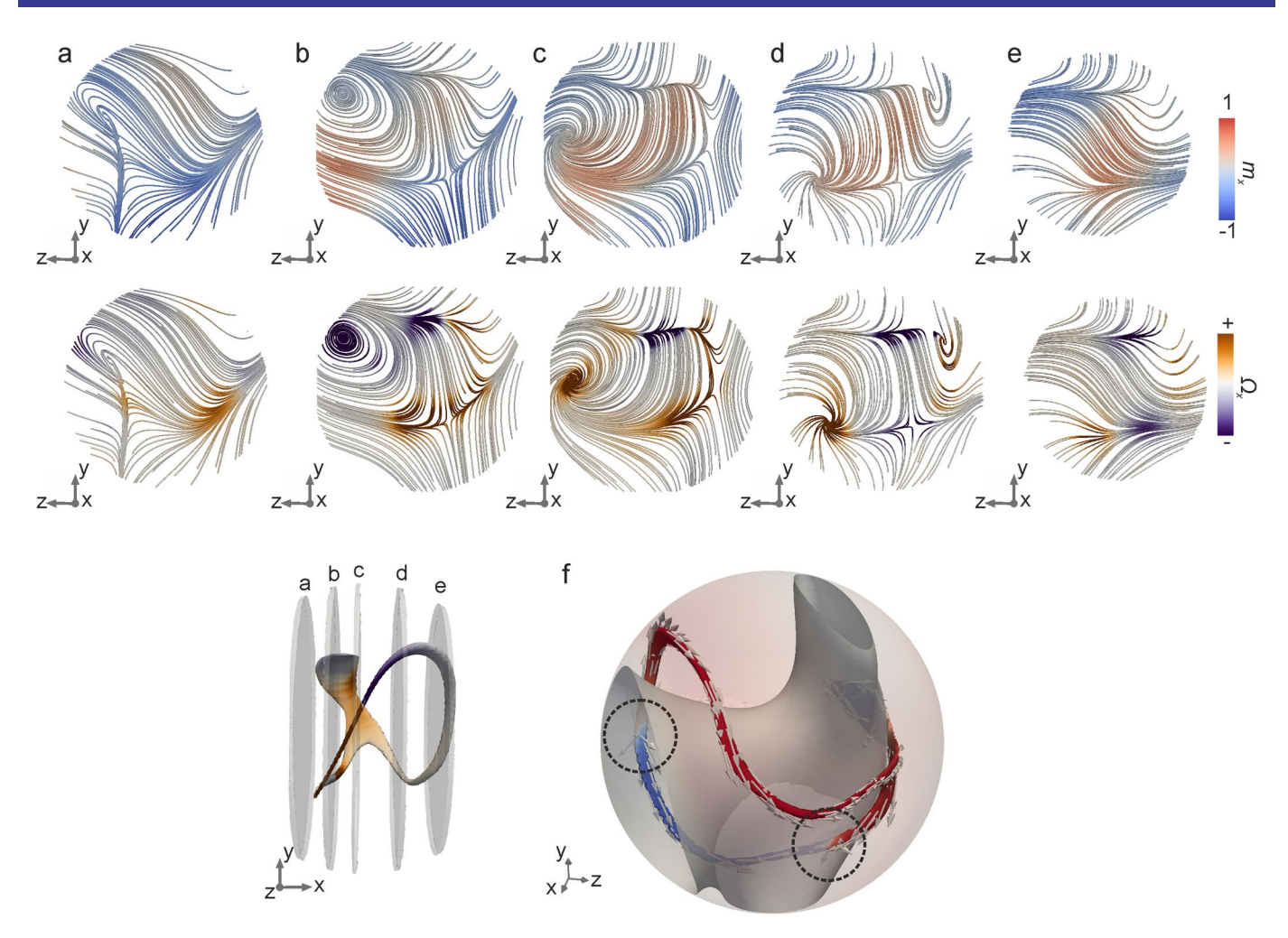
Reprints and permissions information is available at www.nature.com/reprints.



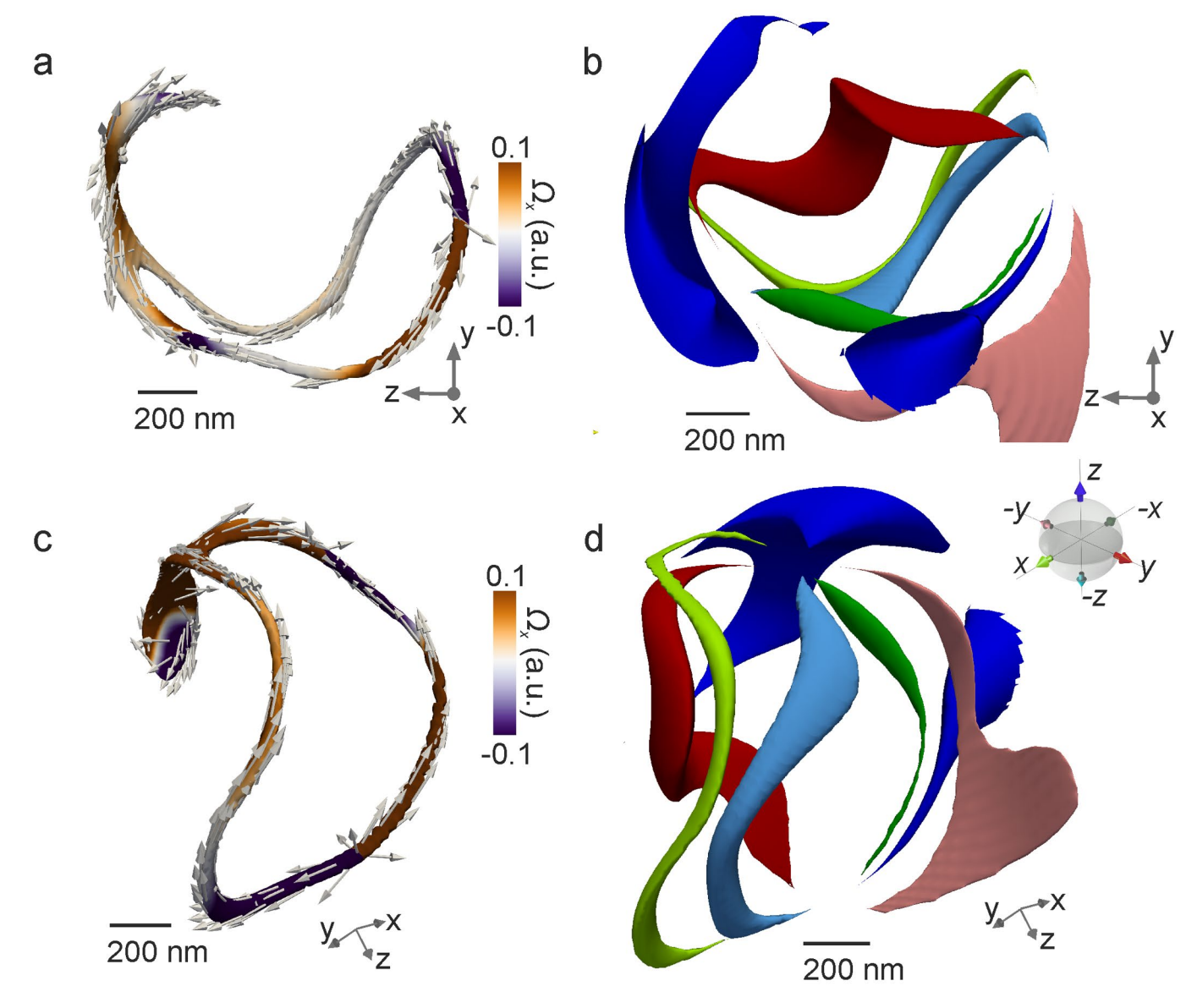
Extended Data Fig. 1 Detailed overview of the vortex ring with circulating magnetic vorticity (presented in Fig. 2), shown in successive slices through the loop. The magnetization within each slice is represented by the streamlines. The colourscale in the top row indicates the \hat{x} component of the magnetization, while the colour scale in the bottom row indicates the \hat{x} component of the vorticity. The vorticity associated with the vortex structure extending throughout the pillar changes sign in slice d due to the presence of a Bloch point, while the vortex-antivortex pair conserves its vorticity throughout. In slices b and c, the magnetization forms a structure similar to that of a cross-tie wall, which dissolves as the pair unwinds, at slices a and d, resulting in a single vortex.



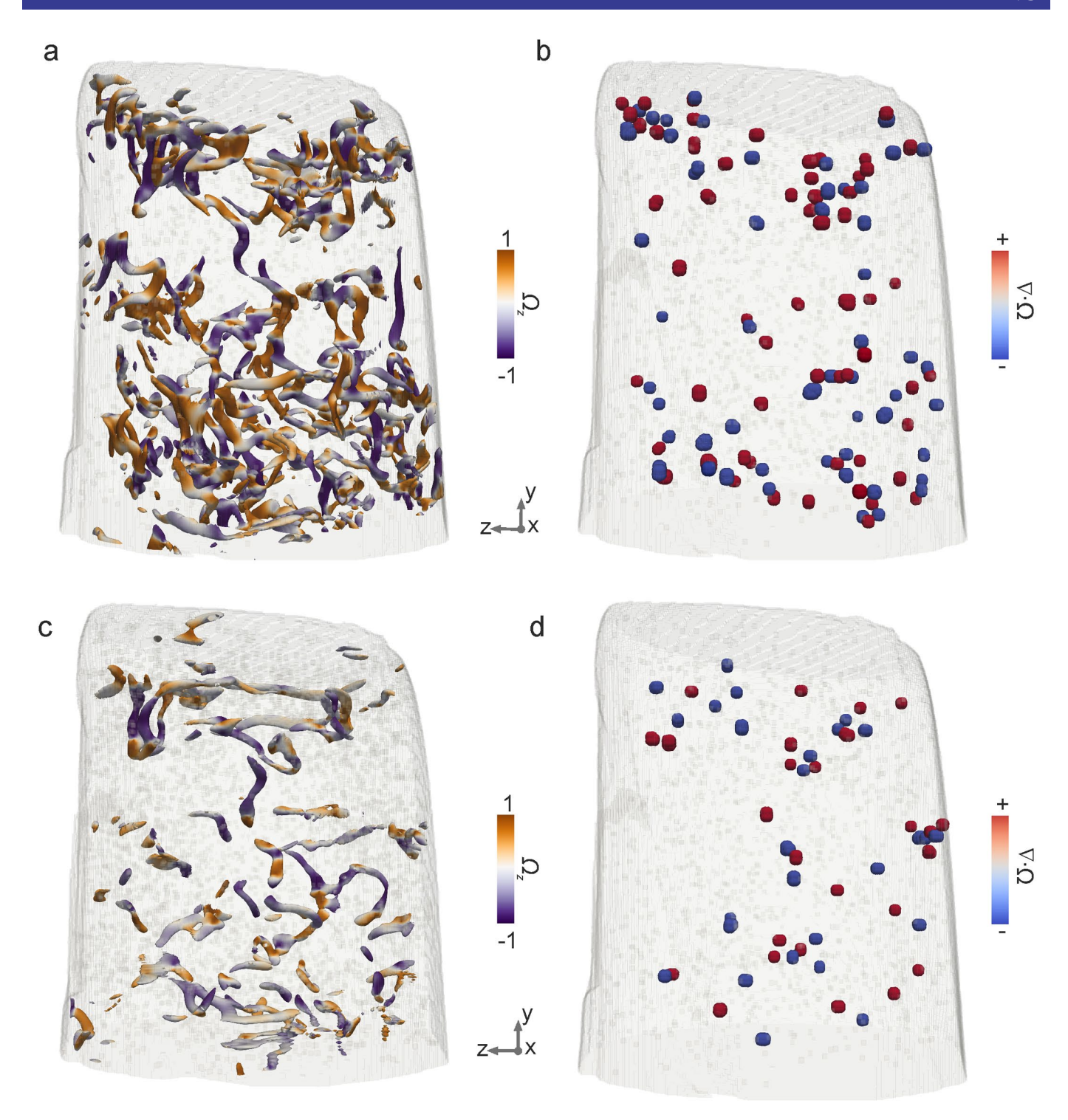
Extended Data Fig. 2 | Analytical models of vortex loops with different magnetization structures. Top, middle and bottom rows: Magnetization, pre-images and vorticity distribution for the different 2+1 dimensional analytical models. The magnetization plots (top row) only include the projection of the magnetization onto the shown plane, while the rings correspond to the positions of the vortex and antivortex centres. The colour indicates the m_z component of the magnetization. The pre-images are shown as volumes where the magnetization vectors deviate only slightly from certain directions \mathbf{d}_{ir} indicated by the colour-coded arrows on each corresponding sphere. The opacity and colour on the vorticity plots indicate the magnitude of local vorticity vectors. The structure in \mathbf{c} is comparable to the vortex rings in Fig. 2, while the structure in \mathbf{d} is comparable to that in Fig. 3.



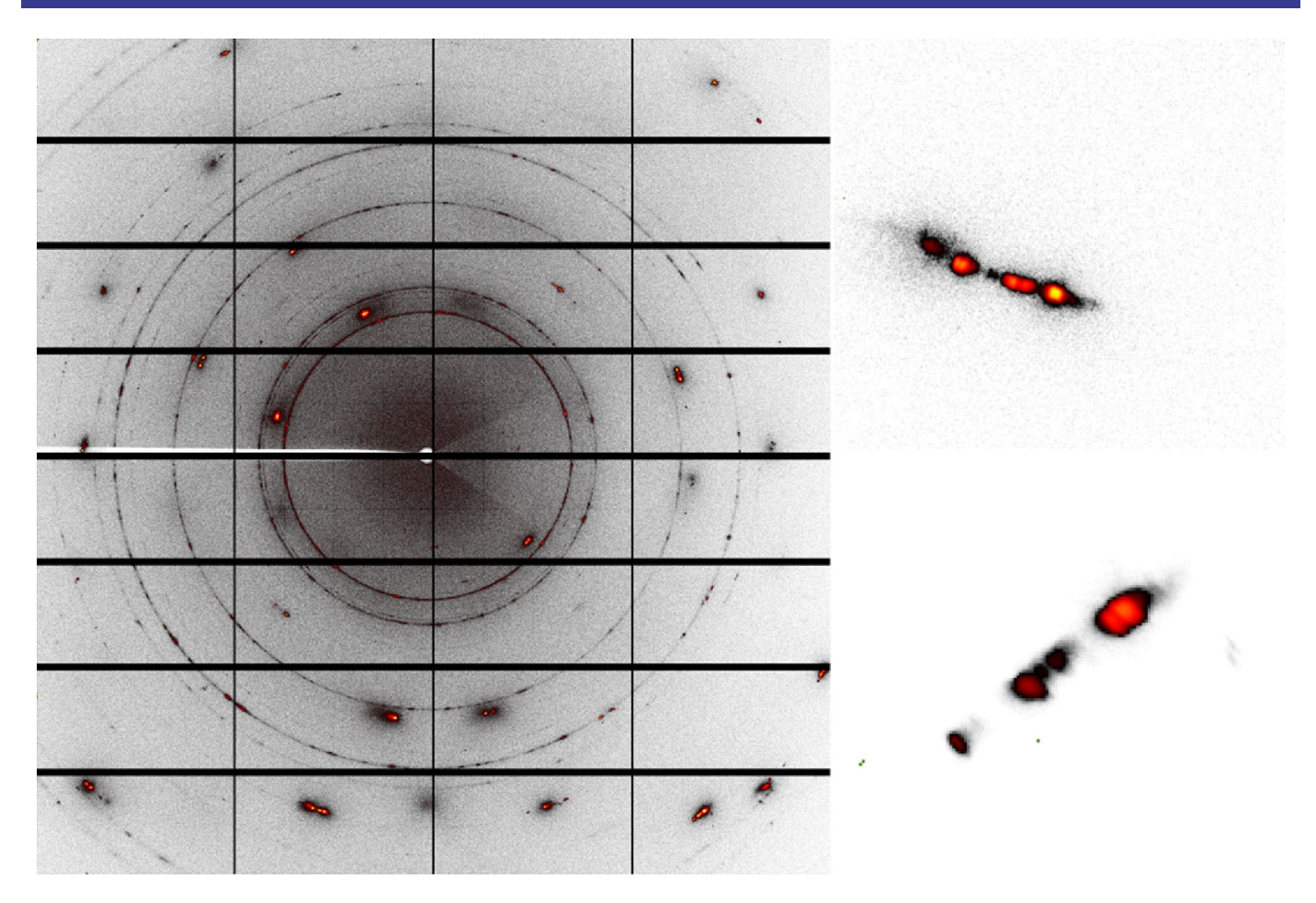
Extended Data Fig. 3 | Detailed overview of the magnetic state of the vortex loop containing Bloch points (presented in Fig. 3), shown in successive slices through the loop. The magnetization within each slice is represented by the streamlines. The colour scale in the top row indicates the \hat{x} component of the magnetization, while the colourscale in the bottom row indicates the \hat{x} component of the vorticity. The vorticity along the vortex core reverses between slices b and c, while the vorticity along the antivortex core reverses between slices c and d. **f**, The white isosurface, plotted along with the vortex loop, corresponds to m_x =0 and separates regions of m_x =+1 and m_x =-1, thus highlighting the presence of a complicated domain wall structure. The Bloch points are located at the intersection of the loop with this isosurface (locations indicated by the dashed circles).



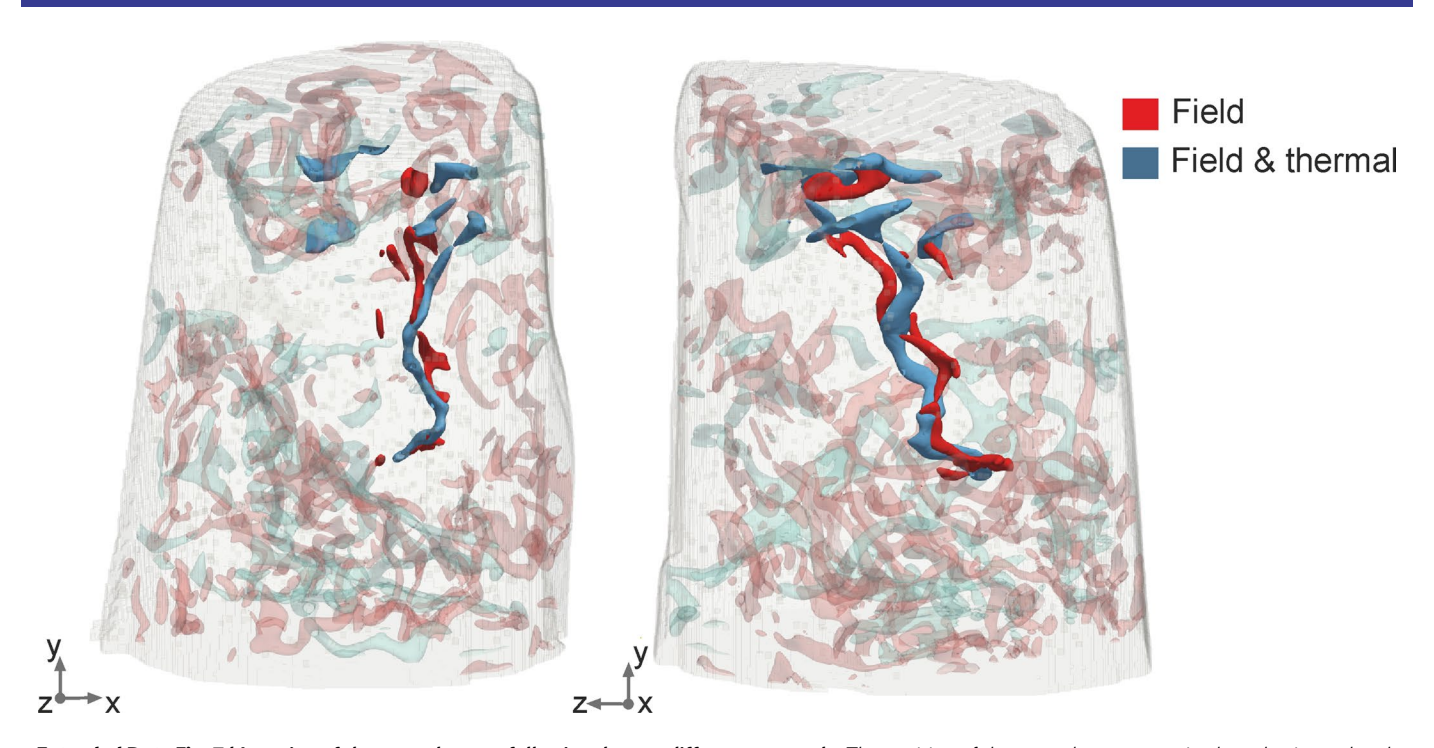
Extended Data Fig. 4 | The vortex loop containing magnetization singularities (presented in Fig. 3) seen from multiple directions. The vortex loop containing Bloch points is plotted using the isosurfaces $m_x = \pm 1$ (**a,c**) and pre-images (**b,d**). In **a** and **b**, the vortex loop and its pre-images have the same spatial orientation as in Fig. 3a. In **c** and **d**, the loop and pre-images are presented with the same orientation as in Fig. 3g.



Extended Data Fig. 5 | Effect of different field and thermal protocols on the presence and distribution of regions of high magnetic vorticity, and magnetization singularities. a,c, Vorticity distribution following the application of a 7 T saturating field (a) and following saturation and field cooling (c).
b, Regions of high divergence of the magnetic vorticity indicate the presence of Bloch points (red) and anti-Bloch points (blue) at remanence, following saturation. d, In the same way, singularities are identified after heating at 400 K and field cooling in a 7 T field. Noticeably fewer magnetic structures with high vorticity are present following the field-cooling procedure.



Extended Data Fig. 6 | A diffraction pattern from the GdCo₂ pillar. The substructure of the Bragg peaks, magnified in the inset to the right, indicates the polycrystalline nature of the material.



Extended Data Fig. 7 | Location of the central vortex following the two different protocols. The position of the central vortex core is plotted using red and blue isosurfaces for the remanent magnetic structure after (red) the application of a 7 T magnetic field, and after (blue) the application of the field-cooling protocol. After both protocols, the vortex core occupies almost the same position.